Japanese Journal of Applied Physics

The Japan Society of Applied Physics

REGULAR PAPER

Ultrasonic measurement of thickness of carotid arterial wall using its natural longitudinal displacement

To cite this article: Yoshifumi Nagai *et al* 2023 *Jpn. J. Appl. Phys.* **62** SJ1039

View the article online for updates and enhancements.

You may also like

- Automated detection of arterial wall boundaries based on correlation between adjacent receive scan lines for elasticity imaging
Yukiya Miyachi, Hideyuki Hasegawa and Hiroshi Kanai

- Accurate Estimation of Carotid Luminal Surface Roughness Using Ultrasonic Radio-Frequency Echo
Kosuke Kitamura, Hideyuki Hasegawa and Hiroshi Kanai

- Arterial wall mechanical inhomogeneity detection and atherosclerotic plaque characterization using high frame rate pulse wave imaging in carotid artery disease patients *in vivo*
Grigorios M Karageorgos, Iason Z Apostolakis, Pierre Nauleau et al.

This content was downloaded from IP address 130.34.32.223 on 12/04/2023 at 04:44

Japanese Journal of Applied Physics **62**, SJ1039 (2023) **REGULAR PAPER**
https://doi.org/10.35848/1347-4065/acba26

Ultrasonic measurement of thickness of carotid arterial wall using its natural longitudinal displacement

Yoshifumi Nagai[1], Shohei Mori[2*], Mototaka Arakawa[1,2], and Hiroshi Kanai[1,2]

[1]*Graduate School of Biomedical Engineering, Tohoku University, Sendai 980-8579, Japan*
[2]*Graduate School of Engineering, Tohoku University, Sendai 980-8579, Japan*

[*]E-mail: mori@tohoku.ac.jp

Received November 15, 2022; revised January 30, 2023; accepted February 7, 2023; published online March 21, 2023

The thickness of the carotid arterial wall obtained from B-mode imaging using ultrasonic diagnostic devices is widely used for the diagnosis of atherosclerosis. However, the measurement interval in the lateral direction of the B-mode image depended on the beam interval (>100 μm). Therefore, the B-mode image is discrete in the lateral direction and cannot reflect changes in local and minute thicknesses. A method for measuring the roughness of the luminal surface of the wall was proposed using the displacement of the carotid arterial wall in the lateral direction during one heartbeat. In this method, the lateral measurement interval is much shorter than the beam interval, enabling a smooth measurement of the luminal surface. By simultaneously applying the method to the lumen-intima and medial-adventitia boundaries of the wall, we propose a novel method to measure the local and minute thicknesses of the carotid arterial wall. © 2023 The Japan Society of Applied Physics

1. Introduction

Circulatory diseases, such as stroke and myocardial infarction, are cited as major causes of death worldwide,[1] and the incidence of such diseases is increasing in Japan.[2] Atherosclerosis is considered the main cause of circulatory diseases; therefore, the early diagnosis and prevention of atherosclerosis are important. Atherosclerosis is known to progress gradually with age;[3] therefore, long-term observation is required. There are several methods for diagnosing atherosclerosis, including computed tomography (CT), magnetic resonance imaging (MRI), arteriography, angioscopy, intravascular ultrasound, and the measurement of arterial walls using ultrasound. Ultrasound is effective because it is non-invasive for the diagnosis of lifestyle diseases.[4–6] Many studies have assessed ultrasound application to various organs such as the blood vessels,[7] heart,[8,9] liver,[10] blood,[11] skin,[12] and bones.[13] Many research have been conducted on high-intensity focused ultrasound therapy[14] and its safety.[15]

Many ultrasonic studies involving measuring the properties of the intima-media complex (IMC) have been conducted to evaluate the degree and state of progression of atherosclerosis.[16–21] At present, the IMC thickness (IMT) of the carotid arterial wall measured using B-mode imaging is regarded as an indicator for diagnosis with a high level of evidence,[22–24] demonstrating its importance in the diagnosis of atherosclerosis.[25–28] Regarding IMT measurement on a B-mode image,[29,30] an echo from the carotid artery in the longitudinal cross-sectional view was acquired using a linear probe and the boundary was detected for each beam position, as illustrated in Fig. 1. Therefore, the measurement interval in the lateral (longitudinal) direction depended on the beam interval (greater than or equal to 100 μm in conventional ultrasonic diagnostic devices). Because the beam interval is generally larger than the sampling interval (approximately 20 μm) in the axial (beam or depth) direction at a sampling frequency of 40 MHz, the results in the lateral direction are more discrete than those in the axial direction, and a change in thickness smaller than the beam interval cannot be measured with high accuracy.

As a simple method for measuring luminal surface roughness of the posterior wall of the artery using ultrasound, a long-axis image of the blood vessel was visualized, as shown in Fig. 1. The depth profile was obtained by mechanically moving the ultrasound probe along the artery or scanning the ultrasonic beam.[20] The sound wave speed in soft tissues between the skin directly under the probe and the anterior wall of the artery is heterogeneous by approximately 10%. Consequently, measurement errors up to several hundred microns could occur when measuring the distance from the probe to the lumen surface. Thus, measuring surface roughness of several microns on the luminal surface is not possible.

It has been reported that the carotid arterial wall could be displaced not only in the axial direction but also in the lateral direction toward the heart during the cardiac cycle.[31–33] Using the natural lateral displacement of the carotid arterial wall, our group proposed a method[34,35] to measure the minute roughness of the wall that occurs in the early stages of atherosclerosis as follows. The blood vessels are pulled in the direction of the heart by cardiac contraction as shown in Fig. 1. However, at this time, soft tissues between the skin and the anterior wall of the blood vessel remain in place: only the blood vessels slide. Using this motion, we aimed to improve the accuracy of surface roughness measurement while keeping each beam of the ultrasonic probe fixed. Figure 2 shows the schematic diagram of the measurement method used. When the blood vessel moves by Δx in the lateral direction during time ΔT, measurement position at the luminal surface also moves by Δx, where the lateral displacement Δx can be estimated by block matching of ultrasonic radiofrequency (RF) signals.[36,37]

Simultaneously, a change of Δd in the distance to the blood vessel wall occurring during time (ΔT) for one ultrasonic beam can also be measured with high accuracy using the phased tracking method.[38,39] Combining temporal changes in these quantities (Δx, Δd), surface roughness can be measured, as shown in Fig. 2. Using this method, the heterogeneity of the sound wave velocity in soft tissues between the skin and anterior wall of the artery is not affected. Therefore, the luminal surface roughness of the posterior wall of the artery can be measured from the skin surface on a range of several microns. This method was

 © 2023 The Japan Society of Applied Physics

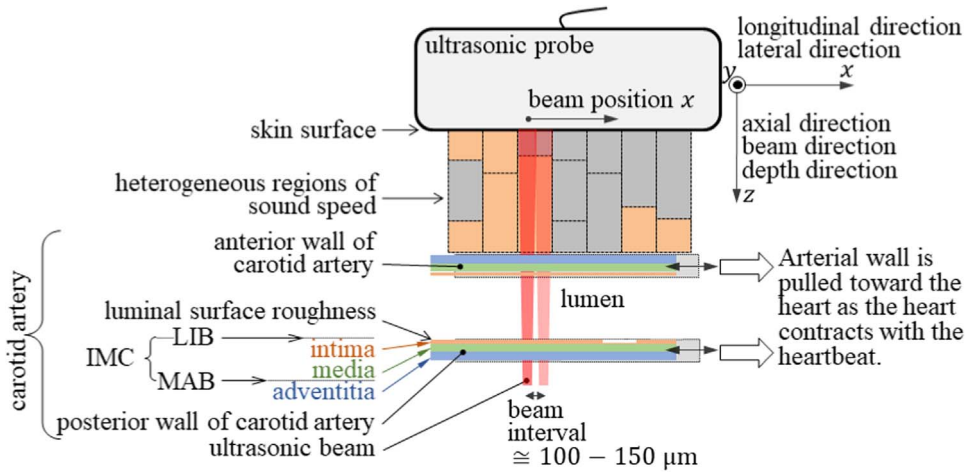

Fig. 1. (Color online) Using the ultrasonic probe for measurement, the related structure of the carotid artery is shown. During one heartbeat, contraction of the heart pulls the carotid artery toward the heart: only the arterial wall slides toward the heart side. The present study employs the phenomena to measure the minute luminal surface and thickness of the intima-media complex (IMC), which is essential for the diagnosis of early stage atherosclerosis.

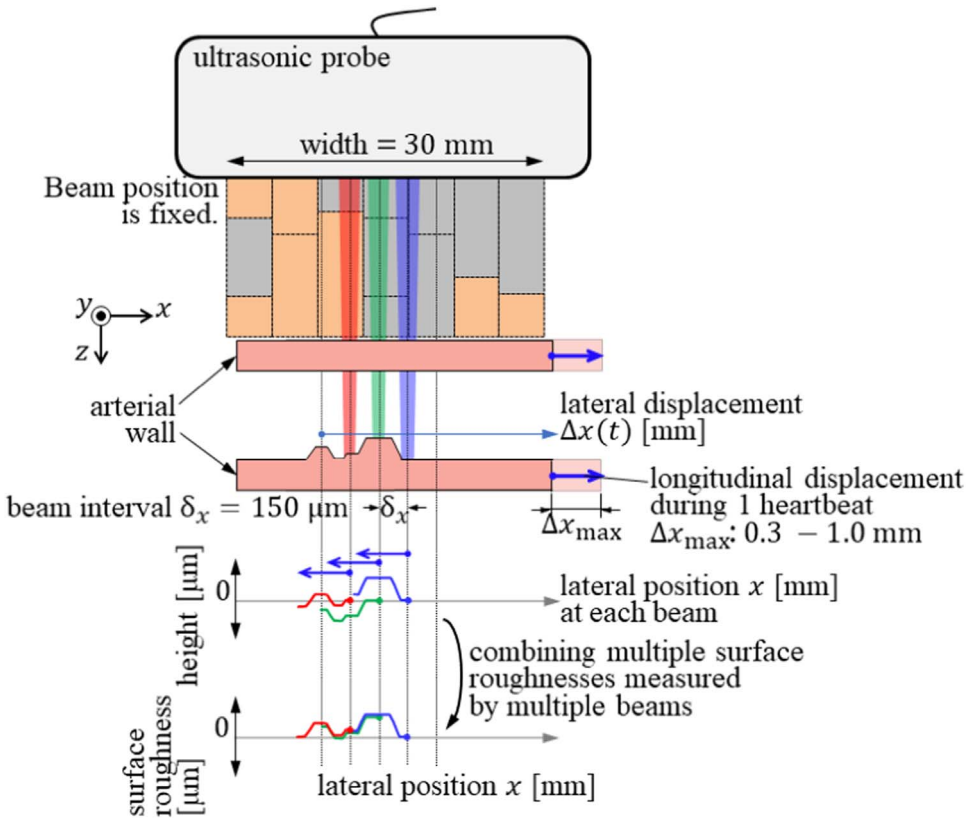

Fig. 2. (Color online) A schematic diagram of the measurement method proposed by our group to measure the luminal surface roughness using ultrasound. The blood vessels are pulled in the direction of the heart by cardiac contraction. However, at this time soft tissues between the skin and the anterior wall of the blood vessel remain in place: only the blood vessel slides. Using this motion, we improve the accuracy of surface roughness measurement while keeping each beam of the ultrasonic probe fixed.

experimentally validated by measuring the surface profile of a silicone tissue-mimicking phantom with a roughness of 13–33 μm height.[40–42]

However, in human individuals, the longitudinal displacement of the arterial wall caused by pulling toward the heart as the heart contracts is small (less than 1 mm), which limits the length of the region that can be measured with a single beam. Kitamura et al. expanded the measurement region by combining multiple surface roughness values measured using multiple beams as shown at the bottom of Fig. 2.[41] In this method, echoes from the arterial wall can be acquired at intervals shorter than the beam interval using the natural displacement of the carotid arterial wall in the lateral direction. Thus, the boundary can be measured smoothly in the lateral direction compared to the method based on B-mode imaging.

In a recent study,[42] we simultaneously applied this method to the lumen-intima boundary (LIB) and media-adventitial boundary (MAB), and the thickness was estimated from the RF signal of all frames of a cardiac cycle. In conventional B-mode images, the measurement interval of the thickness in the lateral direction depends on the ultrasonic beam interval

 © 2023 The Japan Society of Applied Physics

(approximately 100 μm), resulting in discrete and discontinuous results. In contrast, in the proposed method, the carotid arterial wall is effectively scanned using the natural lateral displacement of the carotid artery by fixing the probe position. As the lateral displacements between the frames are much smaller than the beam interval, echoes can be acquired from the wall at short intervals in the lateral direction. Therefore, the estimated thickness becomes smoother in the lateral direction. In the present study, after verification using a tissue-mimicking phantom, the proposed method was applied to in vivo measurements of the carotid artery. Moreover, the thickness estimated using the proposed method was compared with that estimated using conventional B-mode imaging.

2. Principles

2.1. Measurement of surface roughness using natural displacement of arterial wall

Figure 3 illustrates the displacement of the carotid arterial wall (posterior wall) during measurement. As shown on the left-hand side of the figure, the coordinates of the probe are the z' and x' axes in the axial and lateral directions, respectively. At a fixed position of the mth beam on the coordinate system x' on the probe, the wall was longitudinally displaced toward the heart during the systole of the cardiac cycle.

As shown in the figure on the right-hand side, the coordinates of the arterial wall are z and x in the axial and lateral directions, respectively. In coordinate system x on the wall, the lateral position of the mth beam moves from $x_m(n)$ at the nth frame to $x_m(n+1)$ at $(n+1)$th frame along the arterial wall. In the proposed method, echoes are acquired over time, and the probe position is fixed using this natural displacement.

Figure 4 shows the actual in vivo data of a healthy subject. Figure 4(a) shows the lateral (longitudinal) displacement $x_m(n)$ of the carotid arterial wall toward the heart during systole. Figure 4(b) depicts the lateral instantaneous displacement $\Delta x_m(n)$ between frames, from which there is a minute displacement of several tens of micrometers. Figure 4(c) shows the global axial displacement $d_g(n)$ of the wall during the cardiac cycle, which corresponds to the expansion of the arterial wall due to the increase in the inner pressure.

As shown on the right-hand side of Fig. 3, considering the coordinates at the wall, the lateral position of the mth ($m = 1, 2, \ldots, M = 62$) beam is displaced by $\Delta x_m(n)$ from the nth frame to the $(n+1)$th frame. The depth of the wall at lateral position $x_m(n)$ is denoted by $z(x_m(n); m)$. The lateral instantaneous displacement $\Delta x_m(n)$ of the wall from the nth frame to the $(n+1)$th frame is given as follows:

$$\Delta x_m(n) = x_m(n+1) - x_m(n). \tag{1}$$

At the position of the mth beam, the axial instantaneous displacement $\Delta d(n; m)$ from the nth frame to the $(n+1)$th frame is denoted as follows:

$$\Delta d(n;m) = z(x_m(n+1);m) - z(x_m(n);m). \tag{2}$$

The estimated $\widehat{\Delta d}(n;m)$ of $\Delta d(n;m)$ was measured using the phased tracking method.[33] The axial displacement $d(n; m)$ from the 0th frame to the nth frame is given by the accumulation of displacements $\{\Delta d(n;m)\}$ as follows:

$$\hat{d}(n;m) = \sum_{n'=0}^{n-1} \Delta d(n';m). \tag{3}$$

Let us divide $\hat{d}(n;m)$ into the global axial displacement owing to the expansion of the wall, $d_g(n;m)$, and the axial displacement due to the surface roughness of the wall, $d_s(n;m)$, as follows:

$$\hat{d}(n;m) = d_g(n;m) + d_s(n;m). \tag{4}$$

To obtain $d_s(n;m)$, it was necessary to estimate $d_g(n;m)$. Because the measurement region in the lateral direction is as small as approximately 9 mm, compared with the wavelength (approximately 10^2 mm) of the pulse wave, we can assume

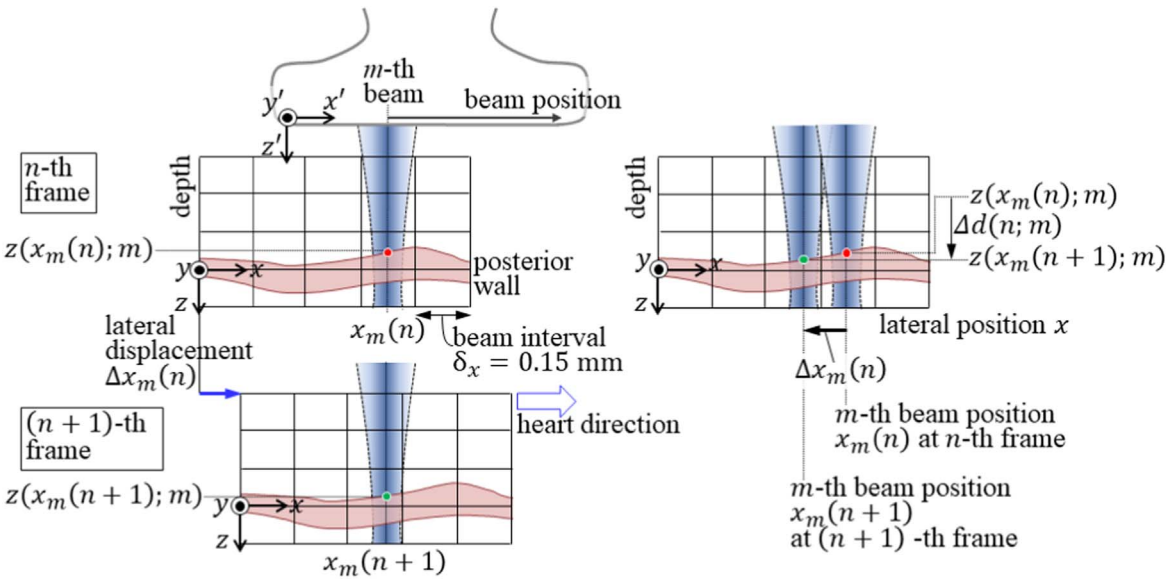

Fig. 3. (Color online) Displacement $\Delta x_m(n)$ of the carotid arterial wall for mth beam during the measurement. Left-hand side: along the coordinate system (x', y', z') on the ultrasonic probe. Right-hand side: along the coordinate system (x, y, z) on the arterial wall.

© 2023 The Japan Society of Applied Physics

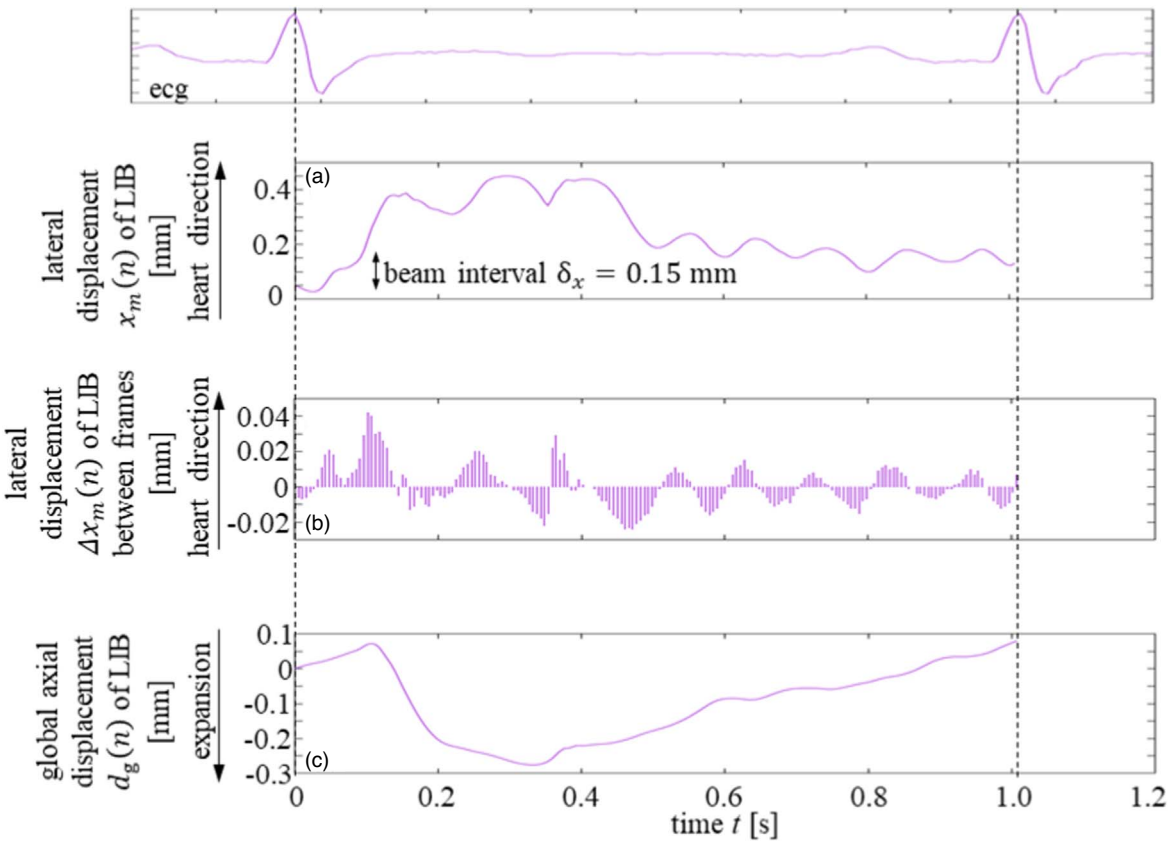

Fig. 4. (Color online) Upper: Electrocardiogram (ECG). (a) Lateral displacement $x_m(n)$ of the carotid arterial wall (LIB) during a cardiac cycle. (b) Instantaneous lateral displacement $\Delta x_m(n)$ between frames of the carotid arterial wall (LIB) during a cardiac cycle. (c) Global axial displacement $d_g(n)$ of the carotid arterial wall (LIB) during a cardiac cycle.

that $d_g(n;m)$ is constant regardless of the beam position, and can be expressed by $d_g(n)$, which is obtained by the accumulation of the spatial average of the axial instantaneous displacements $\widehat{\Delta d}(n;\,m)$ as

$$\widehat{d_g}(n) = \sum_{n'=0}^{n-1} \widehat{\Delta d_g}(n'), \tag{5}$$

where

$$\widehat{\Delta d_g}(n) = \frac{1}{M}\sum_{m=0}^{M-1} \widehat{\Delta d}(n;\,m), \tag{6}$$

where M is the number of ultrasonic beams used for measurement. The estimated $\widehat{d_g}(n)$ value in Eq. (5) is removed from $\hat{d}(n;\,m)$ in Eq. (4) to obtain the surface roughness $\widehat{d_s}(n;\,m)$ of the wall as follows:

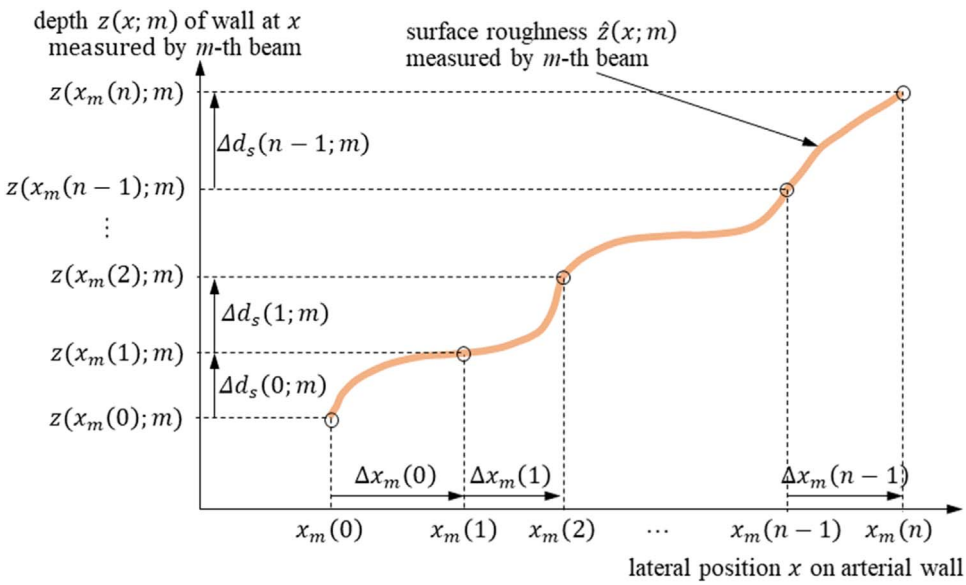

Fig. 5. (Color online) Surface roughness $\hat{z}(x;\,m)$ along the coordinate system (x, y, z) on the arterial wall measured by a single beam (mth beam).

© 2023 The Japan Society of Applied Physics

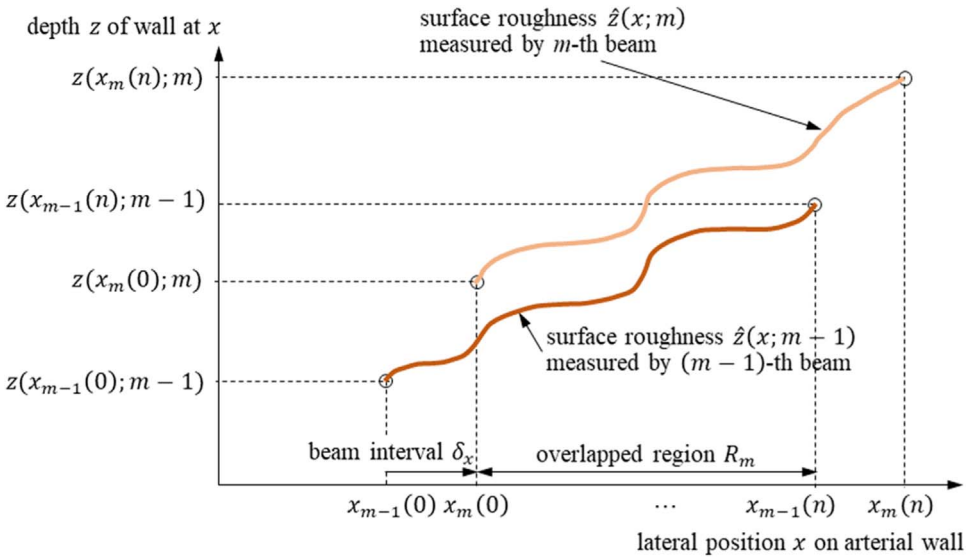

Fig. 6. (Color online) Overlapped measurement region R_m between the surface roughnesses $\hat{z}(x;\ m-1)$ and $\hat{z}(x;\ m)$ measured by $(m-1)$th beam and mth beam.

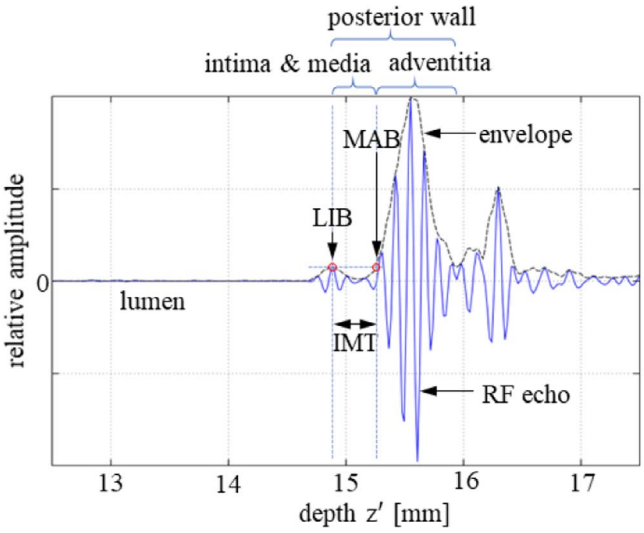

Fig. 7. (Color online) RF echo acquired from the carotid artery and its envelope signal around the posterior wall, by which the LIB and the MAB were determined.

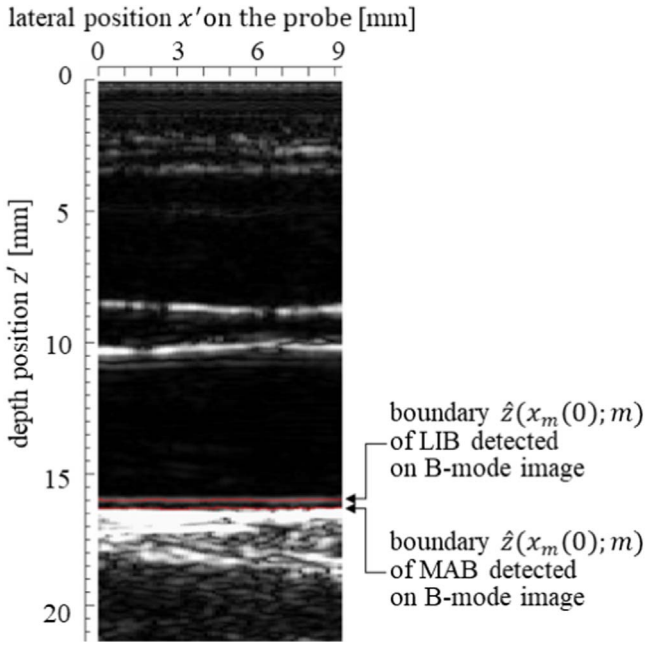

Fig. 8. (Color online) B-mode image of the carotid artery and detected boundaries of LIB and MAB based on the amplitude of echoes.

$$\widehat{d_s}(n;\ m) = \hat{d}(n;\ m) - \widehat{d_g}(n). \tag{7}$$

To obtain $\widehat{d_s}(n;m)$ from Eq. (7), $\hat{d}(n;m)$ of Eq. (4) and axial instantaneous displacement $\Delta d(n;m)$ of Eq. (2) is required. To obtain $z(x_m(n);m)$ of Eq. (2), the lateral direction displacement $x_m(n)$ at the nth frame is determined from the accumulation of the instantaneous displacements $\{\Delta x_m(n)\}$ of Eq. (1) as follows:

$$x_m(n) = \sum_{n'=0}^{n-1} \Delta x_m(n'), \tag{8}$$

where $\Delta x_m(n)$ can be estimated by block matching.[36,37]

To estimate the surface roughness $z(x;\ m)$ at the mth beam, the relationship between the instantaneous lateral displacement $\widehat{\Delta x_m}(n)$ and instantaneous axial displacement $\Delta\hat{d}_s(n;m)$ for each frame n was considered as a parameter, as shown in Fig. 5. The lateral position of the mth beam at the 0th frame and its depth are denoted as $x_m(0)$ and $\hat{z}(x_m(0);\ m)$, respectively. Using the axial displacement $d(n;\ m)$ and the lateral displacement $x_m(n)$ obtained from Eqs. (3) and (8), the surface roughness $\hat{z}(x;\ m)$ for the mth beam at x along the wall can be determined using:

$$\begin{aligned}\hat{z}(x;\ m) &\equiv \hat{z}(\widehat{x_m}(n);m)\\ &= \hat{z}\left(\left(x_m(0) + \sum_{n'=0}^{n-1} \widehat{\Delta x_m}(n')\right);m\right)\\ &= \hat{z}(x_m(0);m) + \sum_{n'=0}^{n-1} \widehat{\Delta d_s}(n';m).\end{aligned} \tag{9}$$

As shown in Eq. (9), the measurement interval in the lateral direction is $\widehat{\Delta x_m}(n)$ for $\hat{z}(x;m)$, which is much smaller than the beam interval $\delta_x = 0.15$ mm of the conventional ultrasonic probe, as shown in Fig. 4(b). Therefore, the

© 2023 The Japan Society of Applied Physics

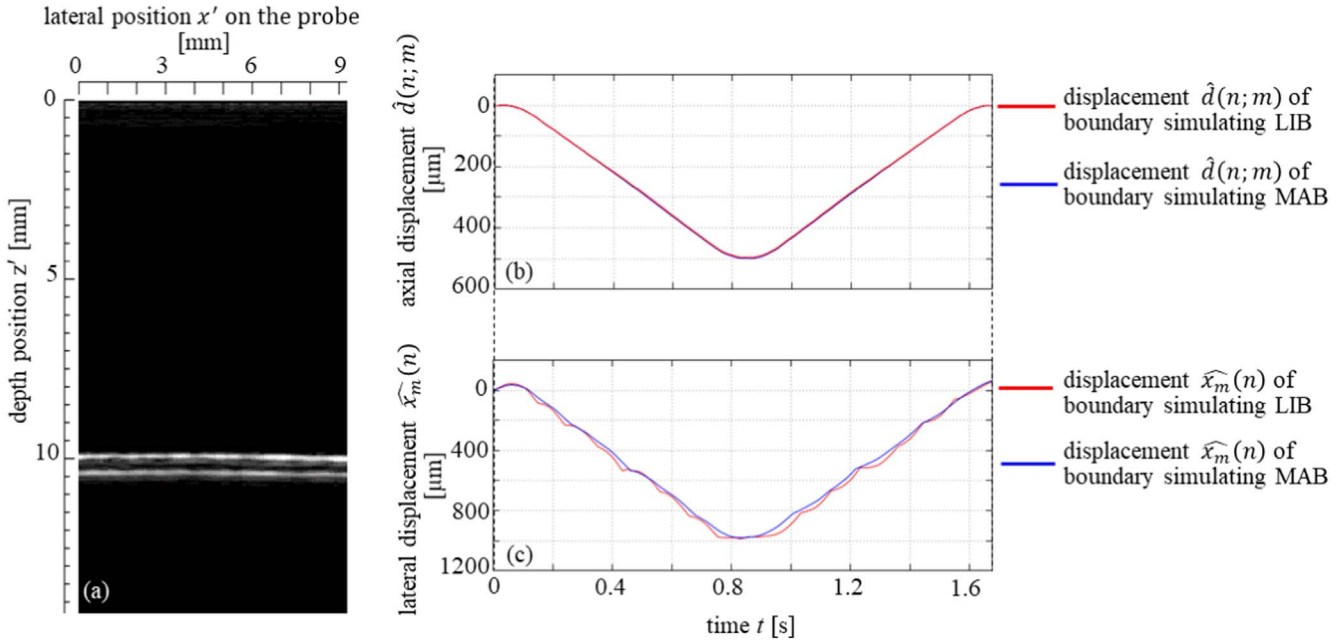

Fig. 9. (Color online) (a) B-mode image of the tissue-mimicking phantom. (b) Axial displacements $\hat{d}(n;\ m)$ for the two boundaries of the two-layer phantom. (c) Lateral displacements $\widehat{x_m}(n)$ for the two boundaries of the phantom.

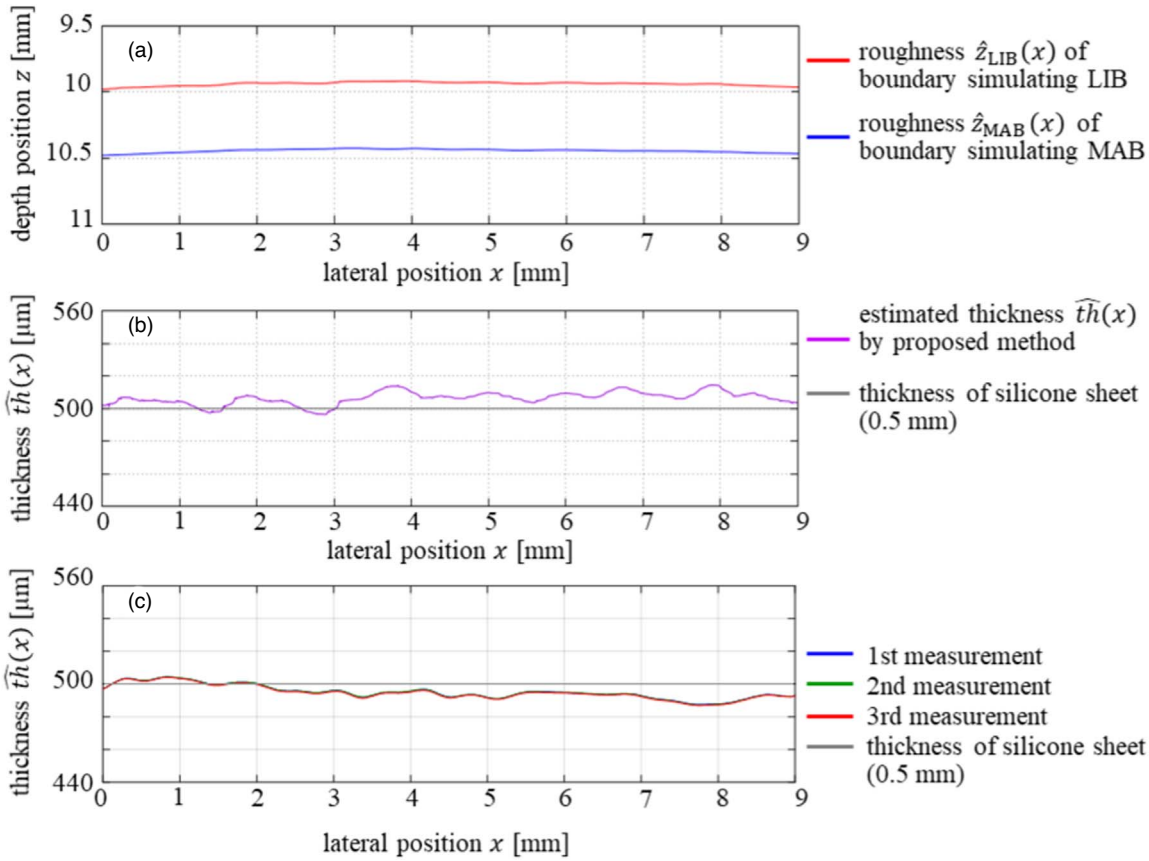

Fig. 10. (Color online) (a) Estimated surface roughnesses $z(x)$ for the two boundaries of the two-layer tissue-mimicking phantom estimated by the proposed method. (b) Thickness $\widehat{th}(x)$ obtained by the proposed method. (c) For the same phantom, the reproducibility in the three measurements of the thickness $\widehat{th}(x)$ was confirmed. The deviation among the three thickness values measured at each lateral position was obtained and their maximum was 0.8 μm.

measurement results obtained using the proposed method were smoother in the lateral direction.

2.2. Combining surface roughness measured by multiple ultrasound beams

The principle for measuring the surface roughness $\hat{z}(x;m)$ using a single beam is described above. Multiple ultrasonic beams were used in the proposed measurement, and the surface roughness was obtained for a wider lateral region, as described below.

Because we assume that the longitudinal displacement of the carotid arterial wall is larger than the beam interval δ_x, the measured roughnesses $\hat{z}(x;m-1)$ and $\hat{z}(x;m)$

 © 2023 The Japan Society of Applied Physics

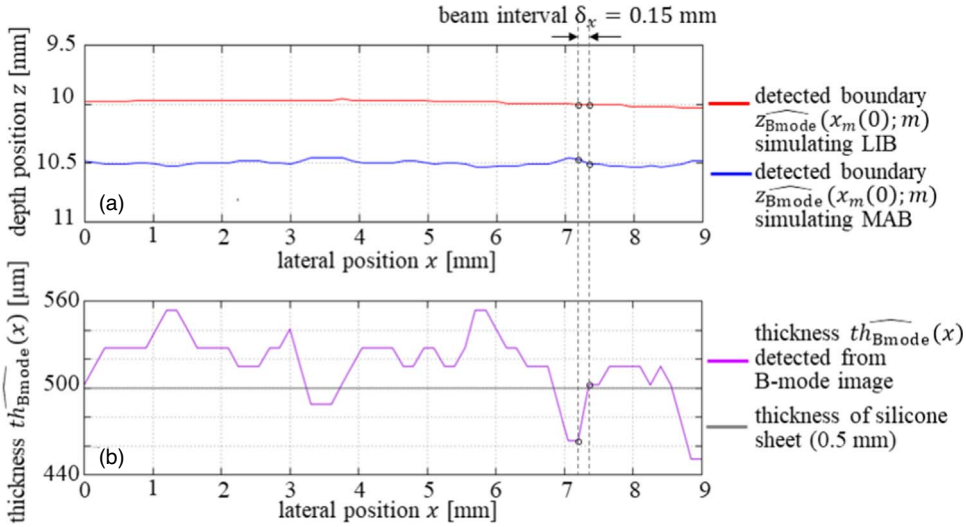

Fig. 11. (Color online) (a) Detected boundary $\hat{z}(x_m(0); m)$ from the conventional B-mode image. (b) Thickness $\widehat{th_{\mathrm{Bmode}}}(x)$[detected from the B-mode image.

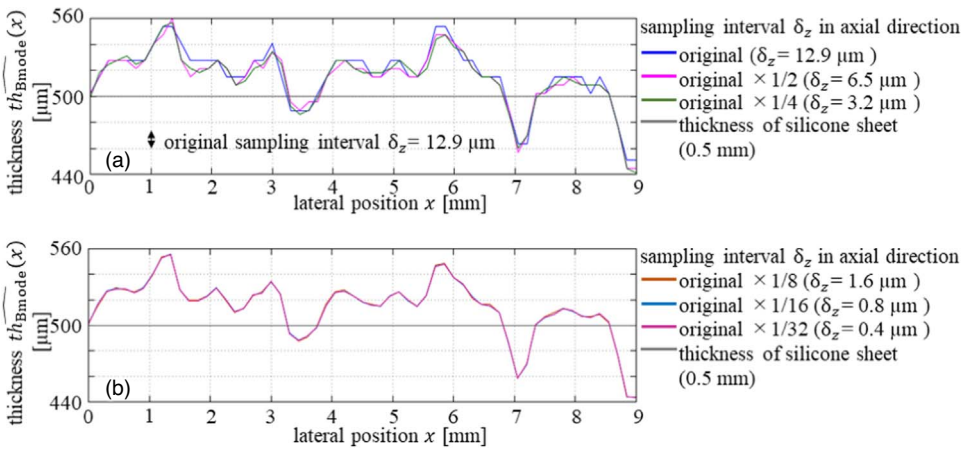

Fig. 12. (Color online) (a) Thickness $\widehat{th_{\mathrm{Bmode}}}(x)$ obtained by the B-mode image for sampling intervals δ_z in the axial direction of 3.2–12.9 μm. (b) Thickness $\widehat{th_{\mathrm{Bmode}}}(x)$ for varying δ_z of 0.4–1.6 μm.

overlap for region R_m along the lateral x-axis, as shown in Fig. 6. As the depths of $\hat{z}(x; m-1)$ and $\hat{z}(x; m)$ do not always coincide because the depth $\hat{z}(x_{m-1}(0); m-1)$ of the arterial surface along the $(m-1)$th beam set at the 0th frame does not match the depth $\hat{z}(x_m(0); m)$ along mth beam set at the 0th frame, the measured roughness $\hat{z}(x; m-1)$ and $\hat{z}(x; m)$ should be adjusted in the axial direction for the overlapped region R_m as follows:

By rearranging the principle described in the previous study,[41] let us minimize the difference of $\hat{z}(x; m)$ from $\hat{z}(x; m-1)$ in the axial direction for the overlapped region R_m to adjust the depth α_m of $\hat{z}(x; m)$. To decide the adjustment depth α_m, the following root mean squared error $\varepsilon_m(\alpha_m)$ is minimized in the region R_m with respect to α_m as follows:

$$\varepsilon_m(\alpha_m) = \sqrt{\frac{1}{N_{m-1,m}} \sum_{x \in R_m} |(\hat{z}(x; m) + \alpha_m) - (\hat{z}(x; m-1) + \widehat{\alpha_{m-1}})|^2}, \quad \text{for } m = 1, 2, \ldots, M \tag{10}$$

where $\widehat{\alpha_0} \triangleq 0$, $\widehat{\alpha_{m-1}}$ for $(m-1)$th beam has already been determined, and $N_{m-1,m}$ denotes the number of the same lateral positions of $\hat{z}(x; m)$ and $\hat{z}(x; m-1)$ included in R_m.

After the depth adjustment, the surface roughness $\hat{z}(x; m)$ of Eq. (9) can be corrected using $\hat{z}(x; m)' \equiv \hat{z}(x; m) + \widehat{\alpha_m}$. Because multiple results $\{\hat{z}(x; m)'\}$ at position of x are measured by multiple beams, the final surface roughness estimate $\hat{z}(x)$ along the wall surface is obtained by averaging the corrected results $\{\hat{z}(x; m)'\}$ at x as follows:

$$\begin{aligned}\hat{z}(x) &= \mathrm{E}_{M_{m,x}}[\hat{z}(x; m)'] \\ &= \mathrm{E}_{M_{m,x}}[\hat{z}(x; m) + \widehat{\alpha_m}],\end{aligned} \tag{11}$$

where $\mathrm{E}_{M_{m,x}}[]$ represents the averaging operation of the corrected surface roughnesses $\{\hat{z}(x;m)'\}$ measured for the ultrasonic beams at the lateral position x.

2.3. Application of surface roughness measurement to thickness measurement of IMT

From the B-mode image, it is known that there is a longitudinal displacement $x_m(n)$ of the carotid arterial wall not only at the depth of the LIB, but also at the depth of the MAB.[33] However, as in previous studies,[40,42] although the

 © 2023 The Japan Society of Applied Physics

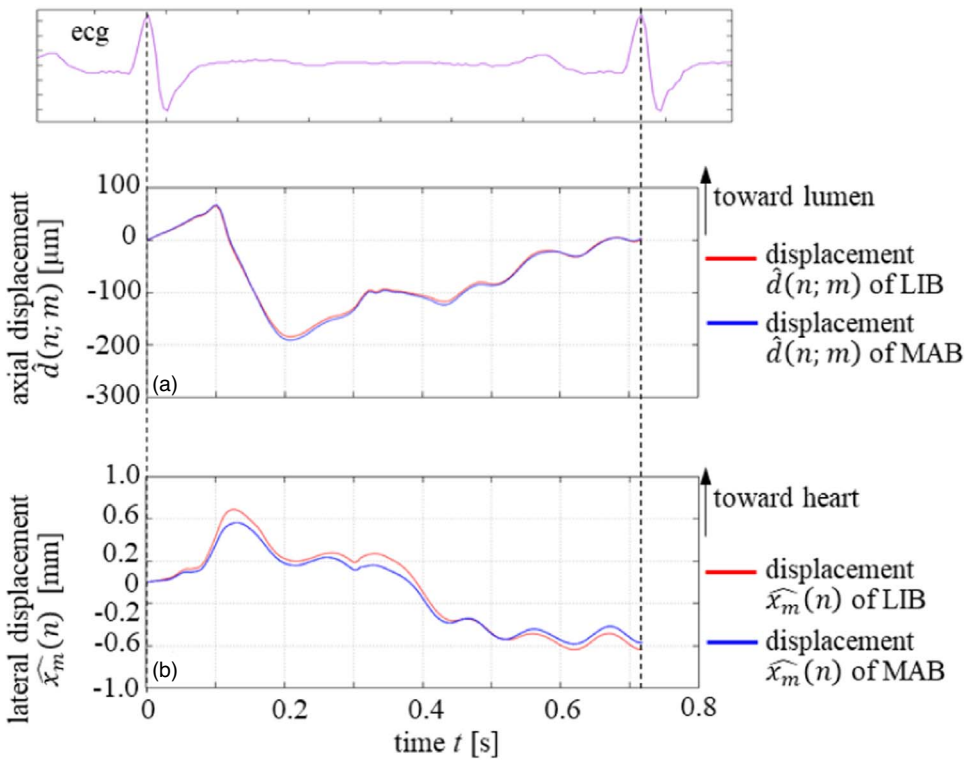

Fig. 13. (Color online) Upper: Electrocardiogram (ECG). (a) Axial displacements $\{\hat{d}(n;m)\}$ for LIB and MAB of the carotid arterial wall. (b) Lateral displacements $\{x_m(n)\}$ for LIB and MAB.

method described in Sects. 2.1 and 2.2 was applied to measure the surface roughness $z_{\mathrm{LIB}}(x)$ of the LIB of the carotid arterial wall, the surface roughness $z_{\mathrm{LIB}}(x)$ of MAB was not measured. In the methods described in Sects. 2.1 and 2.2, the lateral displacement $x_m(n)$ of the object must be larger than the ultrasonic beam interval δ_x. MAB is also applicable because this condition is satisfied.

To estimate the thickness $th(x)$ of the posterior wall of the carotid artery, we simultaneously applied the method described above to measure the surface roughness $z_{\mathrm{LIB}}(x)$ of LIB and that $z_{\mathrm{MAB}}(x)$ of MAB.

For the axial displacement, it is necessary to detect the initial depth $z_{\mathrm{LIB}}(x_m(0);m)$ for the LIB and depth $z_{\mathrm{MAB}}(x_m(0);m)$ for the MAB from the amplitude of the echoes. Figure 7 shows the RF signal (blue) and its envelope signal (dashed line), acquired near the posterior wall of the carotid artery. The amplitude of the echo increased near the LIB and a local maximum was observed between the media and adventitia. In the present study, the initial depth $z_{\mathrm{LIB}}(x_m(0);m)$ of the LIB was determined by detecting the first local maximum by scanning the envelope signal from the lumen to a deeper region. Since the amplitude of the echoes increased again in deeper MAB regions, the initial depth $z_{\mathrm{MAB}}(x_m(0);m)$ of the MAB could be determined by detecting this increase in the envelope signal as follows. When increase in the envelope amplitude is determined by the depth at which the differential waveform reaches the maximum, a deeper portion with a large gradient of the envelope amplitude would be adopted. However, the point, where the amplitude first becomes the lowest at a point deeper than that determined LIB, is susceptible to noise. Therefore, the MAB was determined as a depth deeper than that determined LIB (maximum point of the envelope curve), where the amplitude decreased once, then increased again, and reached the same amplitude as the determined LIB, as shown in Figs. 7 and 8.

Furthermore, the magnitude and speed of the lateral displacements $x_m(n)$ of the LIB and MAB differed.[31] Therefore, it is necessary to independently measure these lateral displacements. In this study, the lateral displacements of the LIB and MAB are estimated by block matching at the depths of the LIB and MAB for each beam position using a window of the same size (lateral direction: 16 points = 2.4 mm, axial direction: 20 points = 372.5 μm).

From the measurements of the surface roughness of LIB $\hat{z}_{\mathrm{LIB}}(x)$ and MAB $\hat{z}_{\mathrm{MAB}}(x)$, the IMT $\widehat{th}(x)$ of the carotid arterial wall is given by

$$\widehat{th}(x) = \hat{z}_{\mathrm{MAB}}(x) - \hat{z}_{\mathrm{LIB}}(x). \tag{12}$$

2.4. Experimental method

Regarding the basic experiment described in Sect. 3, a two-layer tissue-mimicking phantom comprising silicone rubber and a silicone rubber sheet was used to simulate the structure of the carotid arterial wall. A thin sheet (0.5 mm) was used to simulate the IMC, and the surface was roughened using sandpaper (roughness #60) to simulate surface properties at an early stage of atherosclerosis.

Considering the method of making the two-layer phantom, a silicone rubber sheet (IMC simulated phantom) with a thickness of 0.5 mm was spread in a container. Thereafter, liquid silicone (base part) mixed with a hardening agent was poured over the 0.5-mm thick rubber sheet and hardened. Thus, the two layers did not peel in water during the experiment. The surface of the phantom at the base was sticky, which was used to adhere to the metal plate fixed to the motorized stage. Furthermore, the not-measured parts of the phantom and the metal plate were fixed with a rubber

 © 2023 The Japan Society of Applied Physics

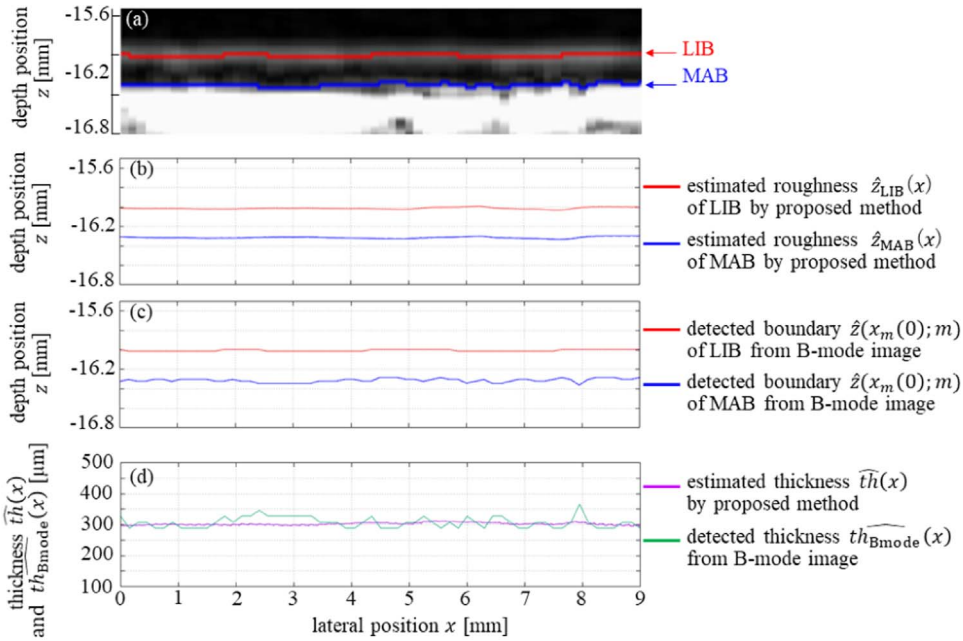

Fig. 14. (Color online) (a) B-mode images of carotid arteries with the detected boundaries of LIB and MAB based on the amplitude of echoes. (b) Estimated surface roughness $z(x)$ by the proposed method. (c) Detected boundary $\hat{z}(x_m(0);\, m)$ from the conventional B-mode image. (d) Thicknesses $\widehat{th}(x)$ and $\widehat{th_{\mathrm{Bmode}}}(x)$ obtained by the proposed method and from the B-mode image, respectively.

band. The sound velocity of the silicone rubber sheet was assumed to be 1030 m s^{-1}. The overall size of the phantom was 65 mm long, 45 mm wide, and 10 mm thick. The water in the tank was degassed by allowing it to stand for one day.

The displacements of the carotid arterial wall in the lateral and axial directions during one cardiac cycle were simulated using a two-axis automatic stage. The two-layer phantom was displaced ±1.0 mm in the lateral direction and ±0.5 mm in the axial direction in a water tank (lateral velocity: 1.4 mm s^{-1} and axial velocity: 0.7 mm s^{-1}). These lateral and axial motions were provided by motorized stages (ALD-906-E1P and ALZ-906-E1P, Chuo-Precision-Industrial Corp. Ltd., Japan). Although $x_m(n)$ on the LIB side is larger than that on the MAB side for in vivo data, as described above, both boundaries were displaced by the same amount in the phantom experiment.

The RF data during this period were acquired with an ultrasonic diagnostic device (Prosound F75, Aloka, Japan) using a linear array probe at 10 MHz (UST-5415, Hitachi Aloka, Japan). The number of beams M was set to 62, beam interval δ_x was 150 μm, frame rate f_{r} was 187 Hz, and sampling frequency f_{s} was 40 MHz. For the in vivo measurements described in Sect. 4, the measurement conditions were the same.

3. Phantom experiment

3.1. Results of phantom experiment

Figure 9(a) presents a B-mode image of the two-layer tissue-mimicking phantom. A two-layer structure simulating the LIB and MAB was visually confirmed. Figures 9(b) and 9(c) show the axial displacements $\hat{d}(n;\, m)$ and lateral displacements $\widehat{x_m}(n)$ at the depths of the LIB and MAB, respectively, measured using the method described in Sect. 2.1.

The surface roughnesses $\hat{z}_{\mathrm{LIB}}(x)$ and $\hat{z}_{\mathrm{MAB}}(x)$ at both boundaries were then estimated, as shown in Fig. 10(a). The thickness $\widehat{th}(x)$ obtained from these results using Eq. (12) is presented in Fig. 10(b), which is approximately 0.5 mm, which is almost the same as the set thickness of the silicone sheet of the tissue-mimicking phantom.

To assess reproducibility of the measurement of the thickness $\widehat{th}(x)$ for the same phantom, the same lateral and axial motions were applied three times by motorized stages, and the results are shown in Fig. 10(c). The experiments in Fig. 10(c) were on a different day from those in Figs. 10(a) and 10(b). The deviation among the three thickness values measured at each lateral position was obtained and their maximum was 0.8 μm, which was sufficiently less than the size (several micrometers) of the disabled cell around the luminal surface of the arterial wall.

3.2. Discussion regarding phantom experiment

Figure 11 shows the thickness $\widehat{th_{\mathrm{Bmode}}}(x)$ of the tissue-mimicking phantom detected from the conventional B-mode image. Figure 11(a) shows the boundary depths $\widehat{z_{\mathrm{Bmode}}}(x_m(0);\, m)$ of the LIB and MAB, which were determined using the same procedure based on the amplitude of the envelope signal, as described in Sect. 2.3 using Fig. 7.

Figure 11(b) shows the thickness $\widehat{th_{\mathrm{Bmode}}}(x)$ obtained from the difference between the results $\widehat{z_{\mathrm{Bmode}}}(x_m(0);\, m)$ in Fig. 11(a). By comparing the thickness estimate in Fig. 10(b) obtained using the proposed method with that obtained using the conventional B-mode image in Fig. 11(b), the estimate in Fig. 10(b) was smoother because its measurement interval in the lateral direction was shorter, as described above.

Meanwhile, for the axial direction shown in Fig. 11(b), the sampling interval in the axial direction of the acquired RF signal was set to $\delta_z \fallingdotseq 13$ μm when the sampling frequency f_{s} was 40 MHz. The spatial resolution of the RF signal envelope was increased in the axial direction to consider the effect of the sampling interval on the estimated thickness, as follows: By interpolating the envelope signal using the reconstruction interpolation method,[43] the sampling interval δ_z was

© 2023 The Japan Society of Applied Physics

equivalently reduced, and then the thickness $\widehat{th_{\mathrm{Bmode}}}(x)$ was updated, as shown in Fig. 12. Although $\widehat{th_{\mathrm{Bmode}}}(x)$ became smoother when δ_z was interpolated up to 1/4 times [green in Fig. 12(a)], the results did not improve when the sampling interval δ_z was further reduced, as shown in Fig. 12(b).

Compared with the conventional B-mode images in Figs. 11(b) and 12, better results were achieved, as shown in Fig. 10(b), that is, close to the true value (500 μm) of the thickness, using the method proposed in Sect. 2.3, for the following reasons:

From the conventional B-mode image, the thickness estimates $\widehat{th_{\mathrm{Bmode}}}(x)$ in Figs. 11(b) and 12 are independently determined for each beam position based on the envelope signal, and the continuity of the measurement results with adjacent beams was not considered. In contrast, in the proposed method, the depth of $\hat{z}(x; m)$ estimated for each beam was adjusted by calculating $\varepsilon_m(\alpha_m)$ using Eq. (10). By adjusting the axial direction, the continuity of the measurement results between the beams is maintained at the estimated roughness $\hat{z}(x)$.

In regard to the 0.5-mm thick rubber sheet used in the phantom experiment, it was difficult to measure the minute change in thickness with the laser displacement sensor. The surface roughness on one side was measured using a laser displacement sensor (LT9010; Keyence Corp. Ltd., Japan) at different five positions, and the standard deviation σ_{L} was 3.3 ± 0.7 μm (average ± standard deviation at five different positions). Thus, the standard deviation of the thickness can be given by $\sqrt{2}\sigma_{\mathrm{L}} = 4.7 \pm 0.9$ μm. On the other hand, for each of the three estimated thickness $\{\widehat{th}(x)\}$ obtained by the proposed method in Fig. 10(c), the standard deviation along the lateral direction was 4.3 μm. Thus, the estimate obtained by the proposed method was close to the actual target value.

Because the ultrasonic beam has a spatial width of several hundred micrometers in the lateral direction, the measurement accuracy in the lateral direction may be degraded. To address this problem, our previous study[42] attempted to suppress the point spread function using a Wiener filter to increase the spatial resolution of the measured surface roughness $\hat{z}(x)$. However, the spatial frequency range in which the improvement was observed was limited to 0–5 mm^{-1}, and further consideration is necessary.

The results of the phantom experiments confirm that the results obtained using the proposed method are closer to the true thickness than those obtained using the conventional method. To further improve the accuracy of the thickness measurement, a method that increases the spatial resolution, which is restricted by the beam width, is required.

4. Results and discussion for in vivo measurement

Ultrasonic RF data were obtained from the carotid artery of a healthy 33 year-old male. The measurement was approved by the Ethics Committee of the Graduate School of Engineering at Tohoku University (No. 19A-5). The participant agreed to participate in this study. The B-mode image is shown in Fig. 8. Figures 13(a) and 13(b) show the axial displacements $\hat{d}(n; m)$ and lateral displacements $\widehat{x_m}(n)$ of the LIB and MAB, respectively, during a cardiac cycle. From Fig. 13(b), it can be confirmed that the lateral displacement $\widehat{x_m}(n)$ of the MAB is larger than the beam interval $\delta_x = 150$ μm.

Figure 14(a) shows a B-mode image near the posterior wall of the carotid artery. Figure 14(b) shows the surface roughness of LIB $\hat{z}_{\mathrm{LIB}}(x)$ and MAB $\hat{z}_{\mathrm{MAB}}(x)$. For comparison, Fig. 14(c) shows the result $\hat{z}(x_m(0); m)$ of the boundary detection of the LIB and MAB from the conventional B-mode image. The arterial wall thicknesses $\widehat{th}(x)$ and $\widehat{th_{\mathrm{Bmode}}}(x)$ obtained from these results [Figs. 14(b) and 14(c)] are shown in Fig. 14(d).

From the thickness estimates of the proposed method, shown in Fig. 14(d), the thickness was smoother than that obtained using the conventional method.

5. Conclusions

In this study, a method for estimating the thickness of the carotid arterial wall was proposed. Using the longitudinal displacement of the carotid arterial wall, the surface roughness of the LIB and MAB was simultaneously estimated using the phased tracking method and block matching. Subsequently, the thickness of the carotid arterial wall was estimated using estimated surface roughness values. Based on the measurement results of the two-layer tissue-mimicking phantom that simulated the structure of the IMC of the carotid arterial wall, the thickness obtained by the proposed method was confirmed to be smoother in the lateral direction and closer to the true thickness compared with the result obtained from the conventional B-mode image. Moreover, the proposed method was applied to in vivo data obtained from the carotid artery of a healthy subject. From the results, we confirmed that the local arterial wall thickness can be measured smoothly using the proposed method compared to the conventional method.

Acknowledgments

This work was supported in part by JSPS KAKENHI 20H02156 and 21H03835.

1) K. J. Foreman et al., Lancet **392**, 2052 (2018).
2) H. Tanaka, M. Nishino, M. Ishida, R. Fukunaga, and K. J. Sueyoshi, Stroke **23**, 946 (1992).
3) F. Ando, K. Takekuma, N. Niino, and H. Shimokata, J. Epidemiol. **10**, 10 (2000).
4) J. T. Salonen and R. Salonen, Circulation **87**, II56 (1993).
5) E. de Groot, G. K. Hovingh, A. Wiegman, P. Duriez, A. J. Smit, J.-C. Fruchart, and J. J. P. Kastelein, Circulation **109**, III-33 (2004).
6) D. S. Celermajer, K. E. Sorensen, V. M. Gooch, D. J. Spiegelhalter, O. I. Miller, I. D. Sullivan, J. K. Lloyd, and J. E. Deanfield, Lancet **340**, 1111 (1992).
7) Y. Shoji, S. Mori, M. Arakawa, S. Ohba, K. Kobayashi, and H. Kanai, J. Appl. Phys. **61**, SG1043 (2022).
8) K. Kawamata, S. Mori, M. Arakawa, and H. Kanai, J. Appl. Phys. **61**, SG1061 (2022).
9) Y. Obara, S. Mori, M. Arakawa, and H. Kanai, J. Appl. Phys. **60**, SDDE02 (2021).
10) W. Saito, M. Omura, J. A. Ketterling, S. Hirata, K. Yoshida, and T. Yamaguchi, J. Appl. Phys. **61**, SG1049 (2022).
11) K. Higashiyama, S. Mori, M. Arakawa, S. Yashiro, Y. Ishigaki, and H. Kanai, J. Appl. Phys. **61**, SG1046 (2022).
12) R. Suzuki, R. Shintate, T. Ishii, and Y. Saijo, J. Appl. Phys. **61**, SG1047 (2022).
13) Y. Maekawa, K. Yano, T. Hattori, and M. Matsukawa, J. Appl. Phys. **61**, SG1019 (2022).
14) N. Obara, S. Umemura, and S. Yoshizawa, J. Appl. Phys. **60**, SDDE04 (2021).
15) T. Aikawa and N. Kudo, J. Appl. Phys. **60**, SDDD13 (2021).

 © 2023 The Japan Society of Applied Physics

16) D. A. Duprez, M. L. De Buyzere, T. L. De Backer, N. Van De Veire, D. L. Clement, and J. N. Cohn, Am. J. Hypertension **13**, 1226 (2000).
17) R. H. Selzer, W. J. Mack, P. L. Lee, H. Kwong-Fu, and H. N. Hodis, Atherosclerosis **154**, 185 (2001).
18) M. C. Corretti et al., J. Am. Coll. Cardiol. **39**, 257 (2002).
19) P. Pignoli, E. Tremoli, A. Poli, P. Oreste, and R. Paoletti, Circulation **74**, 1399 (1986).
20) C. Arihara, H. Hasegawa, and H. Kanai, Jpn. J. Appl. Phys. **45**, 4727 (2006).
21) S. Akiyama, S. Mori, M. Arakawa, and H. Kanai, Jpn. J. Appl. Phys. **60**, SDDA07 (2021).
22) G. L. Burke, G. W. Evans, W. A. Riley, A. R. Sharrett, G. Howard, R. W. Barnes, W. Rosamond, R. S. Crow, P. M. Rautaharju, and G. Heiss, Stroke **26**, 386 (1995).
23) D. E. Grobbee and M. L. Bots, J. Int. Med. **236**, 567 (1994).
24) G. Howard, A. R. Sharrett, G. Heiss, G. W. Evans, L. E. Chambless, W. A. Riley, and G. L. Burke, Stroke **24**, 1297 (1993).
25) J. J. Cao, A. M. Arnold, T. A. Manolio, J. F. Polak, B. M. Psaty, C. H. Hirsch, L. H. Kuller, and M. Cushman, Circulation **116**, 32 (2007).
26) A. Iglesias del Sol, M. L. Bots, D. E. Grobbee, A. Hofman, and J. C. M. Witteman, Eur. Heart J. **23**, 934 (2002).
27) M. Rosvall, L. Janzon, G. Berglund, G. Engström, and B. Hedblad, Atherosclerosis **179**, 325 (2005).
28) M. W. Lorenz, S. von Kegler, H. Steinmetz, H. S. Markus, and M. Sitzer, Stroke **37**, 87 (2006).
29) A. P. G. Hoeks, C. Willekes, P. Boutouyrie, P. J. Brands, J. M. Willigers, and R. S. Reneman, Ultrason. Med. Biol. **23**, 1017 (1997).
30) T. Ishizu, H. Hamaguchi, N. Nitta, Y. Seo, H. Matsuo, and T. Shiina, J. Med. Ultrason. **47**, 155 (2020).
31) M. Cinthio, Å. R. Ahlgren, T. Jansson, A. Eriksson, H. W. Persson, and K. Lindström, IEEE Trans. Ultrason. Ferroelectr. Freq. Control **52**, 1300 (2005).
32) T. Idzenga, S. Holewijn, H. H. G. Hansen, and C. L. de Korte, Ultrason. Med. Biol. **38**, 2229 (2012).
33) M. Cinthio, Å. R. Ahlgren, J. Bergkvist, T. Jansson, H. W. Persson, and K. Lindström, Am. J. Physiol. Heart Circ. Physiol. **291**, H394 (2006).
34) M. Cinthio, H. Hasegawa, and H. Kanai, IEEE Trans. Ultrason. Ferroelectr. Freq. Control **58**, 853 (2011).
35) M. Cinthio, H. Hasegawa, and H. Kanai, 2007 IEEE Int. Ultrason. Symp. Proc.2007997.
36) S. Golemati, A. Sassano, M. J. Lever, A. A. Bharath, S. Dhanjil, and A. N. Nicolaides, Ultrasound Med. Biol. **29**, 387 (2003).
37) J. H. Velduis and G. W. Brodland, Image Vision Comput. **17**, 905 (1999).
38) H. Kanai, M. Sato, Y. Koiwa, and N. Chubachi, IEEE Trans. Ultrason. Ferroelectr. Freq. Control **43**, 791 (1996).
39) H. Kanai, H. Hasegawa, N. Chubachi, Y. Koiwa, and M. Tanaka, IEEE Trans. Ultrason. Ferroelectr. Freq. Control **44**, 752 (1997).
40) Y. Nagai, H. Hasegawa, and H. Kanai, Jpn. J. Appl. Phys. **53**, 07KF19 (2014).
41) K. Kitamura, H. Hasegawa, and H. Kanai, Jpn. J. Appl. Phys. **51**, 07GF08 (2012).
42) Y. Nagai, S. Mori, M. Arakawa, and H. Kanai, Proc. 43rd Symp. on Ultrasonic Electronics (2022), 1Pa5-2, 10.24492/use.43.0_1Pa5-2.
43) I. Céspedes, Y. Huang, J. Ophir, and S. Spratt, Ultrason. Imaging **17**, 142 (1995).

 © 2023 The Japan Society of Applied Physics